



Ocean Wind Field Mapping from Synthetic Aperture Radar and Its Application to Research and Applied Problems

Frank. M. Monaldo, Donald R. Thompson, Nathaniel S. Winstead, William G. Pichel, Pablo Clemente-Colón, and Merete B. Christiansen

APL and the Office of Research and Applications of the National Oceanic and Atmospheric Administration have developed a system to use near-real-time satellite synthetic aperture radar (SAR) data from the Radarsat-1 and Envisat satellites to produce high-resolution (subkilometer) maps of the ocean surface wind field in coastal areas. These maps have shown diverse meteorological phenomena, from gap flows to atmospheric roll vortices. In this article, we describe how SAR can measure wind over the ocean surface and then present examples illustrating how such measurements may be applied. The first application is a scientific one in which SAR wind fields are used to understand the dynamics and spatial variability of barrier jets off the west coast of Canada and the southern coast of Alaska. The second application is a practical one in which high-resolution SAR wind maps are used to determine the optimal placement of offshore wind turbines for generating electric power.

INTRODUCTION

The physics underlying the measurement of marine wind speed from space can be observed by a casual walk to a pond or lake. When no wind is present, the surface of the water is smooth, almost glass-like. As the wind begins to blow, the surface roughens and surface waves begin to develop. As the wind continues to blow more strongly, the amplitude of the waves increases, roughening the surface still more. Careful examination of the wind-generated waves reveals that these surface wave crests are generally aligned perpendicular to the prevailing wind direction.

The scattering of microwave radar pulses from a wind-roughened surface, i.e., the normalized radar cross section (NRCS), is critically dependent on the surface roughness. At moderate incident angles, 20° – 60° from nadir, nearly all of the radar energy directed at a smooth water surface will reflect away from the direction of the incident beam at an angle from the local vertical equal to that of the incident beam, just like optical radiation from a mirror. This is called “specular scattering.” As the surface roughens, however, more of the incident radiation will be reflected back toward the radar,

and the scattering process becomes significantly more complicated.

All available closed-form models for electromagnetic scattering from rough surfaces are asymptotic approximations to an exact solution of Maxwell's equations. The two most commonly used models are the Kirchhoff approximation¹ and the small perturbation method (SPM).² The Kirchhoff approximation is valid when the local radius of curvature of the surface is large compared to the wavelength of the incident radiation. It correctly models quasi-specular scattering but lacks polarization sensitivity. The SPM is valid for small slopes and small surface wavelengths. It yields the proper polarization sensitivity for this regime but does not properly account for long-scale features in the surface roughness spectrum or for specular scattering. In the SPM limit, the backscattered cross section is proportional to the spectral component of the surface roughness spectrum at the so-called Bragg wavenumber, a measure associated with the radar wavelength projected on the surface, or $2k \sin \theta$, where k is the radar wavenumber and θ is the local incident angle. The radar wavenumber equals $2\pi/\lambda$, where λ is the radar wavelength. Microwave radars for measuring wind speed have operated at wavelengths in the centimeter to decimeter range. Surface roughness at these scales is responsible for most of the backscatter.

Recently, a popular approach for developing more accurate approximate analytical scattering models has been to investigate successive iterations of the surface-current integral equation to find a model that is correct for both of the above limits. In fact, several authors have found relatively simple closed-form expressions for the scattered field that satisfy such criteria. (For a detailed discussion of these scattering models and interaction of the surface-current integral equation, see, for example, Refs. 3–6 and references contained therein.)

Clearly, to accurately predict the wind field near the ocean surface from the backscatter NRCS, one needs a detailed understanding of the relationship between the wind vector and the surface roughness spectrum and an accurate scattering model. Although there has been significant progress in explaining the hydrodynamics associated with wind/wave interactions as well as in analytical and numerical scattering physics, for practical applications this relationship is usually determined empirically. One way to determine this “geophysical model function” is to compare NRCS measurements, typically from aircraft, with wind vector measurements from instrumented buoys. These data are then fit to a specified functional form that is flexible enough to characterize the known dependencies. This form can be written as

$$\sigma^0 = u^{\gamma(\theta)} A(\theta) [1 + B(u, \theta) \cos \varphi + C(u, \theta) \cos 2\varphi], \quad (1)$$

where

σ^0 = the NRCS,
 u = the wind speed measured 10 m above the surface,
 φ = the wind direction with respect to the radar look direction,
 θ = the local incident angle, and with

γ , A , B , and C being functions of incident angle and wind speed, and implicitly of the radar frequency.⁷

Note the general behavior of Eq. 1. As wind speed increases, the radar cross section increases exponentially, depending on $\gamma(\theta)$. In terms of angular dependence, the observed NRCS is greatest for $\varphi = 0^\circ$, that is, the wind is blowing toward the radar look direction. The NRCS is smallest when the wind direction and radar look direction are orthogonal, i.e., $\varphi = 90^\circ$. There is another, slightly smaller maximum in the NRCS when the wind is blowing directly away from the radar look direction.

The other salient feature from Eq. 1 is that, for a specific wind speed, wind direction, and radar geometry, it is possible to compute the associated NRCS. Unfortunately, the inversion is not unique. A single NRCS may be associated with a large number of wind speed and direction pairs.

Currently, the wind vector over the ocean is measured operationally by scatterometer satellites like QuikSCAT,⁸ which uses two conically scanning pencil-beam radars directed at slightly different incident angles near 50° . As the radar beams scan, and the satellite travels along its orbit, an 1800-km-wide swath of radar measurements is swept out beneath the satellite. At each point on the ocean, the NRCS is measured at two different incident angles, two polarizations, and, as the beams look forward and aft, two different aspect angles. Taken together these multiple NRCS measurements can be used to determine a unique estimate of wind speed and direction. The spatial resolution of such measurements is 25 km.

If we were only concerned about the behavior of global wind vectors over the global oceans, the problem of wind vector retrieval from space would be solved by QuikSCAT-class satellites. Although such sampling is extremely valuable for monitoring ocean surface winds globally, this relatively coarse resolution misses important phenomena in coastal regions, where the wind fields can vary over spatial scales on the order of a few kilometers or smaller. It is for such applications that we have pursued the exploitation of synthetic aperture radar (SAR) imagery.

The term “synthetic aperture” aptly describes the way a SAR functions. Typically, SARs are side-looking radars, projecting a beam pattern on the surface in the radar look direction (range) and along the SAR flight-path direction (azimuth). Along the range direction, high spatial resolution measurements of the NRCS are made by fine-scale timing of the return radar pulse.

Unlike the case for real aperture radar, for which the azimuth (along-flight-path) resolution is limited by the beamwidth of the antenna, a SAR system synthesizes high azimuth resolution by using Doppler frequency estimates of the returned pulse.

Consider a back-of-the-envelope computation. The angular resolution of an antenna is approximately λ/D , the ratio of the radar wavelength to the antenna size. For a spaceborne system having a 5-cm wavelength and a 10-m aperture, the angular resolution is 0.005 rad. Now assume a typical satellite altitude of 800 km and a look angle of 20° . This results in an 850-km range to the surface. At this range, an angular resolution of 0.005 rad corresponds to a ground resolution in the azimuth direction of more than 4 km. At larger incident angles, the resolution progressively worsens.

A SAR, by contrast, records the magnitude and phase of the backscattered radar pulses as it flies, and later, through processing, creates a much larger “synthetic” antenna. In the previous example, if the radar returns are recorded for 1.5 s (about the time for the spaceborne SAR to fly 10 km), the effective antenna length (through processing) is 1000 times larger. Consequently, the ground azimuth resolution is about 4 m instead of 4 km. In practice, compromises are made to reduce the noise in the measurements. SAR imagery from spaceborne platforms, with orbit parameters similar to those given above, typically yield a 25-m resolution and 100-km-wide swaths. In its wide-swath mode used to measure coastal wind fields, SAR image resolution is typically 100 m, with a 450-km-wide swath.⁹

The SAR achieves much better spatial resolution than a conventional scatterometer, but within a SAR image each NRCS measurement is made at a single incident angle and single aspect angle. There is thus an issue as to how Eq. 1 can be inverted to estimate the wind field. If an estimate of wind direction over the image is somehow available, then Eq. 1 can be inverted using the measured NRCS. At least two ways exist to obtain this *a priori* estimate of wind direction: by using numerical weather forecast models or by examining linear features within the SAR image itself.

The use of numerical weather model predictions is the most straightforward approach. Global numerical models typically make wind direction predictions on a $1^\circ \times 1^\circ$ longitude/latitude grid, whereas local mesoscale models may make predictions on grids as small as 4 km. The wind direction from the model is interpolated down to the location of a SAR image pixel and wind speed retrieval is performed. A wind speed image is produced by performing this

inversion at every pixel in the SAR image. The advantage of using model wind directions for the retrieval is that the data are routinely available and represent a dynamically stable smooth wind field. However, the coarseness of the wind direction field may cause important features to be missed. An alternative and complementary approach is to use linear features present in the SAR image itself to estimate the wind direction. Many SAR images have linear features at spatial scales ranging from several hundred meters to a few kilometers that are generally aligned with the local wind direction.^{10–13} The use of such features to determine wind direction has the virtue of detecting high-resolution wind field changes directly from the SAR image; however, the features are not always present and only determine the direction to within a 180° ambiguity.

APL has implemented a quasi-operational system, both in-house and at the National Oceanic and Atmospheric Administration (NOAA), that combines near-real-time SAR imagery acquired at the Alaska Satellite Facility in Fairbanks and wind direction estimates from the Navy Operational Global Atmospheric Prediction System (NOGAPS) model to provide near-real-time high-resolution wind speed estimates. Comparisons^{14,15} indicate that the wind speed retrievals agree with both buoy and QuikSCAT measurements to better than 1.8 m/s for wind speeds less than 20 m/s.

The process of producing a high-resolution wind speed image is best illustrated with an example. Figure 1 is a



Figure 1. Radarsat-1 SAR NRCS image near Kodiak Island, Alaska. The bright or high cross-sectional areas represent high wind speeds. This image was acquired at 03:44 UTC on 31 October 2000 and was processed by the Alaska Satellite Facility. (Original SAR data courtesy of the Canadian Space Agency.)

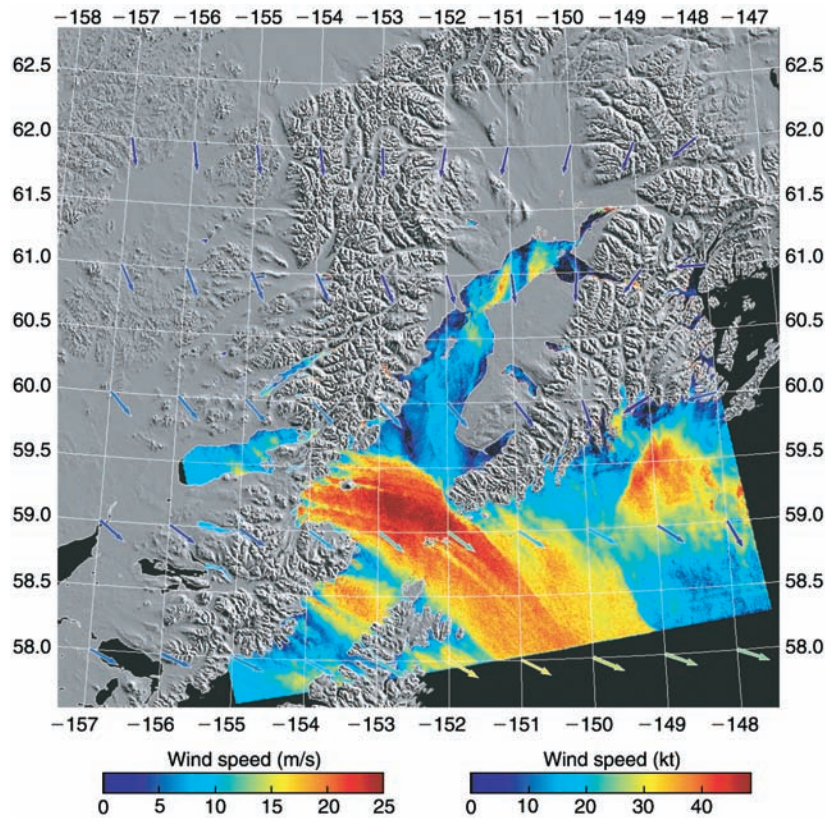


Figure 2. Radarsat-1 SAR wind speed image near Kodiak Island, Alaska. The intensified gap flows, reaching over 20 m/s (40 kt), are responsible for what Alaskans call *williwaws*. This wind speed image was derived from the NRCS image shown in Fig. 1.

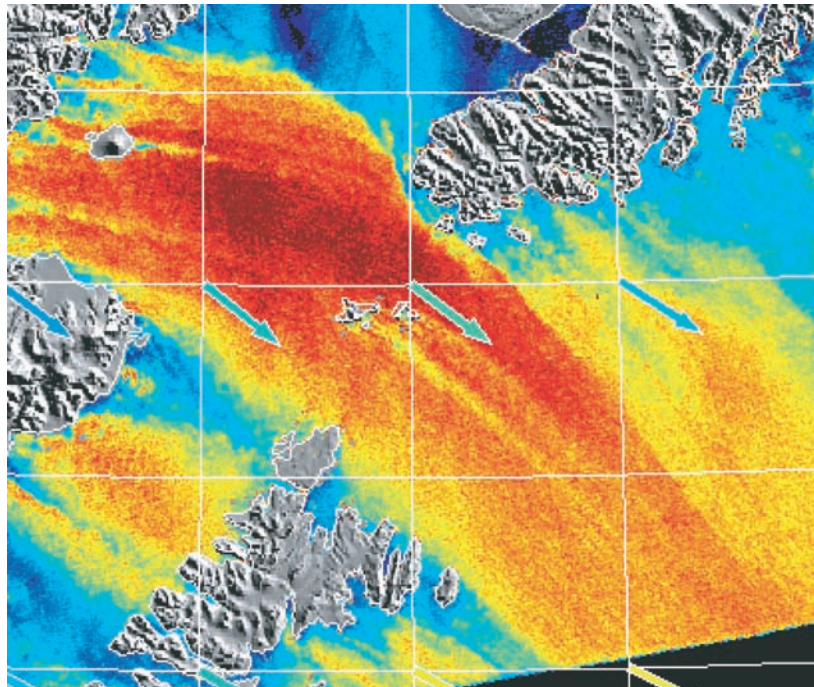


Figure 3. Blowup of the wind speed image from Fig. 2 near the Barren Islands. Note that the wind-shadowing lee of the islands extends for over 100 km.

grayscale representation of a Radarsat NRCS image off the coast of Alaska. The land and water areas are clearly distinguished. Figure 2 represents the color-coded wind speed image produced from this SAR image using model wind directions for the inversions. The land area has been masked with a grayscale-shaded relief map. The arrows at the latitude/longitude grid points represent the model estimates of wind speed and direction. This imagery illustrates important features of wind fields in coastal areas.

Land topography often dramatically affects the marine wind field. The most conspicuous feature of Fig. 2 is the intensification of wind speed as air is funneled through the strait between Kenai Peninsula and Kodiak Island. Alaskans call these local wind speed funnels “blow holes” or “williwaws.” Figure 3 is a blowup of the area around the Barren Islands. Note that wind shadowing by the islands affects the wind field more than 100 km downwind of the islands.

In the next sections we discuss how high-resolution SAR wind maps can be used to study the dynamics of the coastal wind field in ways inaccessible to other instrumentation. We first illustrate the potential for SAR wind mapping for addressing fundamental problems in mesoscale meteorology. This particular example shows how SAR wind maps are being used in a study sponsored by the National Science Foundation (NSF) to investigate barrier jets and gap flows in the Gulf of Alaska. In addition to scientific applications, we also demonstrate how SAR wind mapping may help to answer very practical questions concerning the design and deployment of wind farms for the production of electrical energy from turbines in shallow-water coastal regions.

APPLICATIONS

Mesoscale Meteorology in the Gulf of Alaska

This section examines the use of SAR as an important tool for studying mesoscale meteorological phenomena

in coastal regions around the globe. We focus here on the Gulf of Alaska, where a combination of factors provides a nearly perfect location to study these intense phenomena. Figure 4 shows that the coastal regions around the gulf are ringed by complex terrain with high mountain ranges and multiple gaps. The gaps are important because they provide a path for air masses from interior Alaska to flow into the gulf. In addition, the extratropical cyclone track migrates through the gulf. As a result, frequent landfalling synoptic low-pressure areas and fronts occur throughout the year (especially in fall and winter). These synoptic systems interact with the terrain and with air flowing from interior Alaska through the aforementioned gaps to provide strong mesoscale forcing. This forcing leads to frequent, very high wind events throughout the coastal regions of the gulf. The gaps in the terrain induce a complex horizontal structure within these windstorms. This situation provides the ideal testbed for observing atmospheric phenomena with SAR.

Two specific examples of mesoscale meteorological phenomena that occur frequently in the gulf and are readily observable using SAR are gap flows and barrier jets. Gap flows occur when cold continental air spills through gaps in the coastal terrain (Fig. 2). Barrier jets are described below. Sometimes both types of flow coexist and interact. They are often associated with gale-force, storm-force, and even occasionally minimal hurricane-force winds. Many ships have sunk or experienced severe distress within these flows.¹⁶ Complicating matters further is the case where gap flows and barrier jets interact in complex ways, frequently creating

significant horizontal wind variability that is easily captured by the SAR-generated high-resolution wind maps. In fact, winds within both gap flows and barrier jets often vary from nearly calm to more than 25 m/s over a span of several kilometers. Clearly, such winds pose a significant hazard to marine interests throughout the Gulf of Alaska.

In addition to the meteorological forcing present in the gulf, the high latitudes provide excellent polar-orbiting satellite coverage. With one wide-swath SAR, such as those aboard Radarsat-1 and Envisat, every point along the Gulf of Alaska coast is observed at least once every 1.5 days. On some days, there are two passes (one ascending and one descending), and with two SARs even four passes are possible. NOAA and APL have partnered to take advantage of this coverage by ordering many thousands of SAR image frames from the Gulf of Alaska over an 8-year period (1997–present). This project, the Alaska SAR Demonstration, has provided a wealth of valuable wind data for examining coastal flows in the gulf.¹⁷ With more than 30,000 high-resolution wind snapshots available from Alaskan coastal waters, the potential for basic research into coastal flows over an otherwise data-sparse region is enormous. The following discussion illustrates how these data are being applied to gain insight into the structure and dynamics of barrier jets (with an emphasis on their interaction with gap flows) in the Gulf of Alaska.

Barrier jets (Fig. 5) occur when a stable atmospheric flow encounters a barrier in the local terrain.¹⁹ The traditional conceptual model of the atmospheric response is as follows. If the flow is sufficiently statically stable (resistant to vertical motion), it is blocked from crossing the barrier. As mass accumulates along the upwind side of the barrier, a pressure ridge (i.e., an ageostrophic, local, positive-pressure perturbation) is induced that aligns parallel to the terrain barrier. The atmosphere adjusts to this imbalance by deflecting the onshore flow to the left (Northern Hemisphere) and accelerating it down this pressure gradient. In the far field (down the barrier), the flow becomes rotationally trapped against the barrier because the Earth's rotation (Coriolis force) forces the flow right, but the mountain barrier and the static stability block it. The resulting flow morphology in this classical model is an exponential increase in speed, with a gradual turning of the wind along and upwind of the barrier.^{20,21}

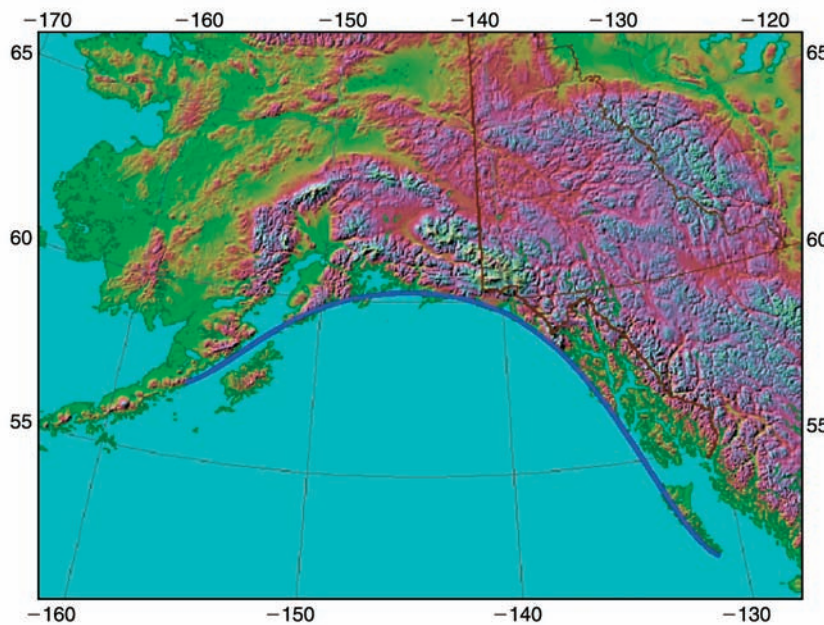


Figure 4. Shaded relief map of the Gulf of Alaska. The 6th-order polynomial fit used to derive the plots in Fig. 6 is shown.

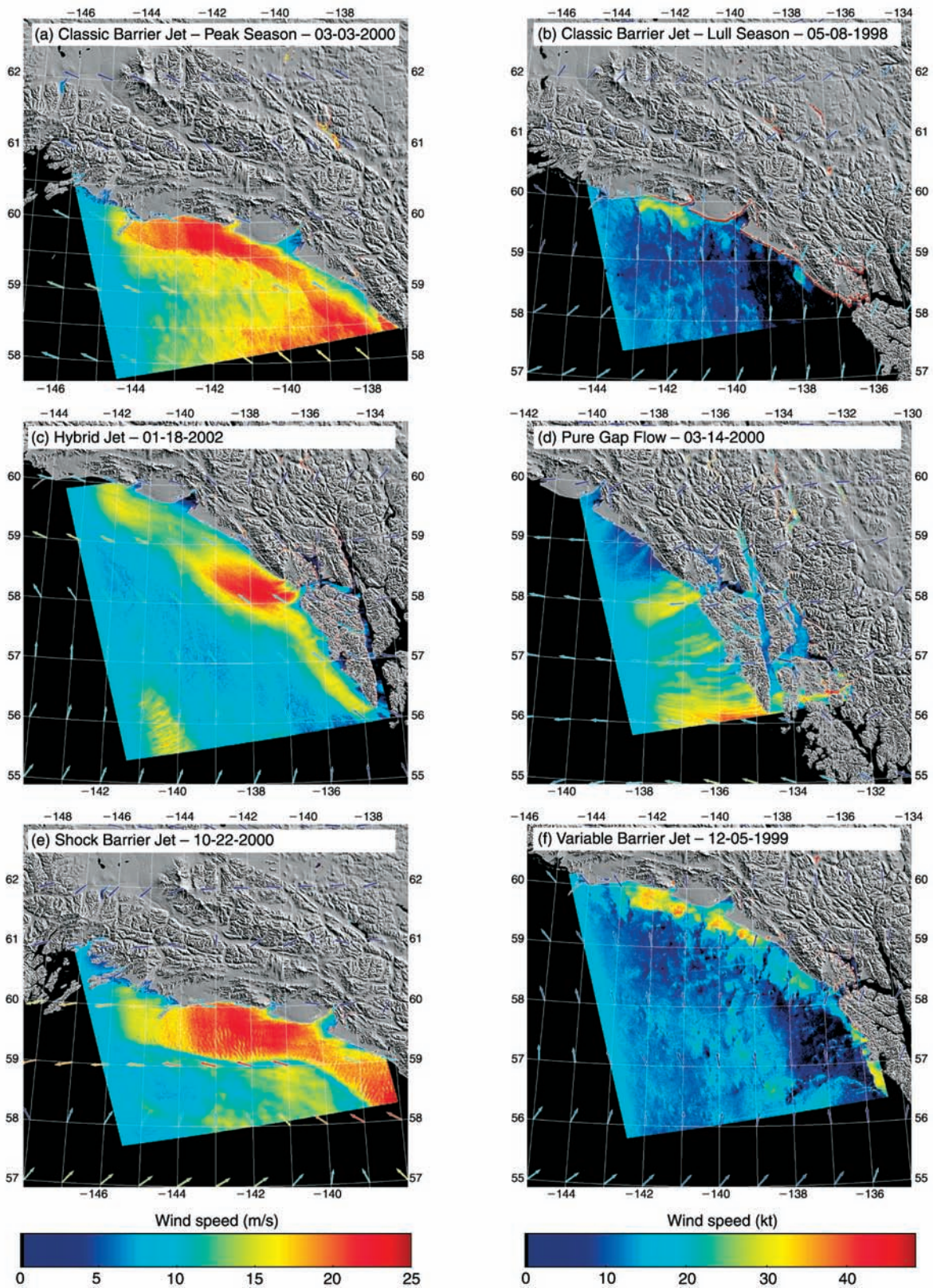


Figure 5. SAR-derived surface wind speed analysis. (a) A classic barrier jet. The shore-parallel band of red shading is the jet. (b) A lull season barrier jet. Notice the slower ambient flow and weaker barrier jet. (c) A hybrid jet. The gap flow can be seen exiting the first gap from the right of the image and rapidly turning parallel to the shore. (d) Pure gap flow. The yellow streaks of enhanced wind speed are oriented perpendicular to the shore, indicating that the offshore-directed gap flow is not turning coast-parallel. (e) A shock barrier jet with a large wind speed gradient on the outer edge. (f) A variable barrier jet. Note the “lumpy” appearance of the jet hugging the coastline. (Reprinted, with permission, from Ref. 18: © 2005, the American Meteorological Society.)

These flows have been well studied, and barrier jets have been observed along the Appalachian mountains (so-called cold air damming²¹), along the West Coast of the United States (including California^{22,23}), and along the Washington and Oregon coasts.²⁴ In addition, such events have long been known to occur in the Gulf of Alaska as well.¹⁶ In all cases, however, many of the details regarding these flows and their underlying dynamics have remained unknown because of the inability to observe them. In the past, barrier jet observations have been limited to *in situ* aircraft flights. Although these flights yield local data, the context within which the flow occurs has heretofore been missing. Mesoscale numerical weather prediction models have helped fill the gap, but the nature of numerical modeling has its own set of limitations. Additional observations are needed.

The snapshots provided by SAR imagery have provided significant new insight into these types of flow. For example, SAR images of barrier jets in the Gulf of Alaska show that classical barrier jet theory does not explain the types of barrier jets that occur there. Figure 5 shows several barrier jets: two classic jets (a, b), one hybrid jet (c) with characteristics of both gap flow and classic barrier jet, one shock jet (e) characterized by a very sharp offshore wind speed gradient, and one variable jet (f) characterized by significant variability in the along-jet direction. All of these jets are located between Mount Fairweather and Prince William Sound. It is immediately evident from these examples that very sharp offshore wind speed gradients can be associated with these structures (Fig. 5e), gap flows feeding into these jets play an important role in their morphology, and other jets exist that are highly variable in the along-coast direction. This morphology is not consistent with the exponential wind speed increase predicted by classical barrier jet theory. However, this sort of feature has been observed before by research aircraft and has long been part of the experience of local mariners in Alaska.²⁵ Access to SAR images in this region has confirmed and provided context to these previous observations. Of course, such observations of sharp gradients and other nonclassical features lead one to ask what the governing dynamics are that cause these features. Once these dynamics are understood, can techniques for forecasting the strength and shape of these phenomena be

developed? Such questions led to a proposal to study barrier jets in the Gulf of Alaska.

The Mesoscale Dynamic Meteorology program at the NSF recently funded a multi-institution team of investigators to use SAR, aircraft, and mesoscale model data to gain insight into outstanding issues. The team was tasked to

- Document the over-water details of the surface wind structures of barrier jets using SAR and other *in situ* instrumentation
- Explore barrier jet dynamics using modeling, SAR, and aircraft observations
- Transfer this knowledge to forecasters near the Gulf of Alaska

The team is currently 2 years into this 3-year project, and substantial progress has been made at achieving these objectives. Specifically, in terms of documentation, a 5-year SAR climatology of barrier jets has provided some important new insights into barrier jet occurrence (frequency and location) in the Gulf of Alaska.^{18,26} In addition, a new class of barrier jets called “hybrid jets” has been discovered. These are barrier jets whose morphology is clearly influenced by the intrusion of air from gaps in the coastal terrain. Figure 5c shows an example of a barrier jet that meets this definition. One important finding is that several gaps and bays serve as important source regions for hybrid jets. Figure 6 shows this relationship and is a plot of barrier jet occurrence as a function of location along the coastal function (shown in Fig. 4). Several geographical features (including the

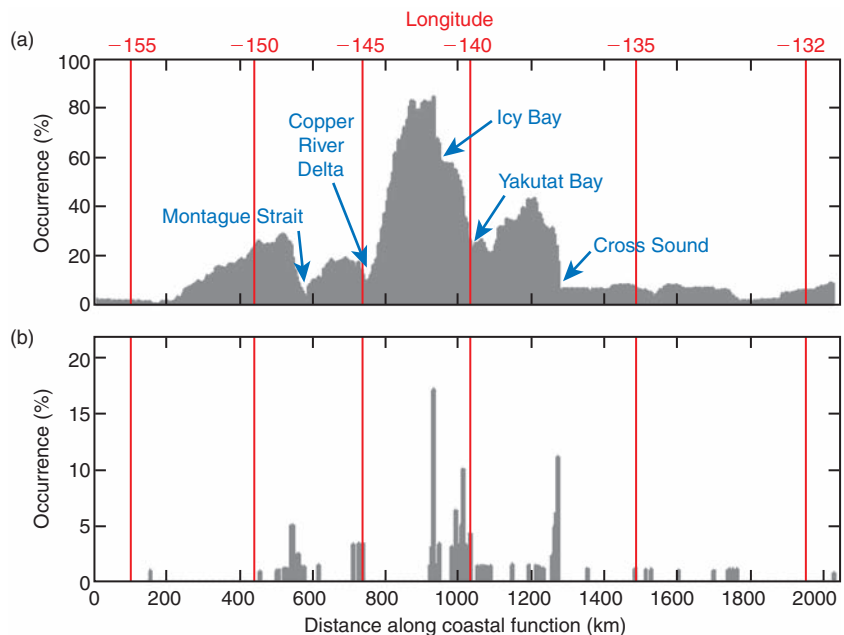


Figure 6. Percentage occurrence of barrier jets as a function of location (a) along the Gulf of Alaska coast and (b) at the starting point of the jets. The statistics were computed along the coastal-fitting function shown in Fig. 4.¹⁸

Copper River Delta, Icy Bay, Yakutat Bay, and Cross Sound) are important source regions for these hybrid barrier jet features. The implications for mariners are clear: If one is going to sail downwind of one of those gaps, one needs to be aware of the conditions that lead to the development of the often severe winds associated with these hybrid flows.

Wind Energy Development

Offshore wind energy production is developing rapidly in Europe, and optimistic goals are set for the future implementation of large-scale wind farms. Some advantages of installing wind turbines offshore include higher mean wind speed and reduced turbulence compared to land sites. Large turbines on high towers can be implemented offshore with minimal visual and noise disturbance. The largest turbines operating today can generate 2.1 MW of power, but the trend is toward higher-capacity and deeper-water installations. Currently, wind farm construction is limited to near-shore areas where the water depth is relatively shallow (i.e., less than 20 m).

Wind turbine power output increases with the cube of the mean wind speed. Therefore, wind farms must be carefully situated according to observations of the regional wind climate.²⁷ Figure 7 is a wind speed map

generated from an ENVISAT ASAR (advanced SAR) scene obtained in wide-swath mode over Denmark. Arrows representing NOGAPS wind vectors indicate that winds are from the southwest, which is the prevailing wind direction in the area. Significant variations of wind speed occur, particularly between the eastern and western parts of the Danish waters, possibly caused by a front. In addition to the wind climate, wind farm siting is based on water depth, visual impact, wildlife habitats, bird migration, and convenience for connecting to the electrical grid.

To quantitatively estimate the wind energy potential at a given location, one needs a sufficient number of observations of wind speed and direction to account for diurnal and seasonal changes in the wind field. In addition, all wind directions must be represented. Typically, meteorological measurements are made each hour over a full year and observations of wind speed are grouped into intervals of wind direction. A probability density function is then used to describe the mean wind speed, variance, and energy density.²⁷

Erecting and maintaining a meteorological mast offshore is costly; therefore, remote sensing techniques are attractive, as wind farm development is moving from land to sea. At Risø National Laboratory in Denmark, work is ongoing to produce reliable predictions of wind

energy potential from satellite SAR observations.^{28,29} Between 60 and 70 randomly selected SAR images are required to estimate mean wind speed with a 10% uncertainty at a 90% confidence level.³⁰ Estimates of variance and power density require 150 and 2000 images, respectively.

One shortcoming of SAR measurements with respect to wind statistics for a given site is that they are obtained at fixed times of the day because of the near-polar satellite orbit. The absolute accuracy of SAR-derived wind speed is lower than *in situ* measurements, but SAR measurements are very useful in the early planning of offshore wind farms when *in situ* measurements are not available.³¹

For offshore wind farms already in operation, there is interest in determining their effect on the local wind climate. Such information is needed for environmental impact evaluations and also for siting new wind farms in clusters. Since the most ideal offshore sites are occupied, new wind farms are

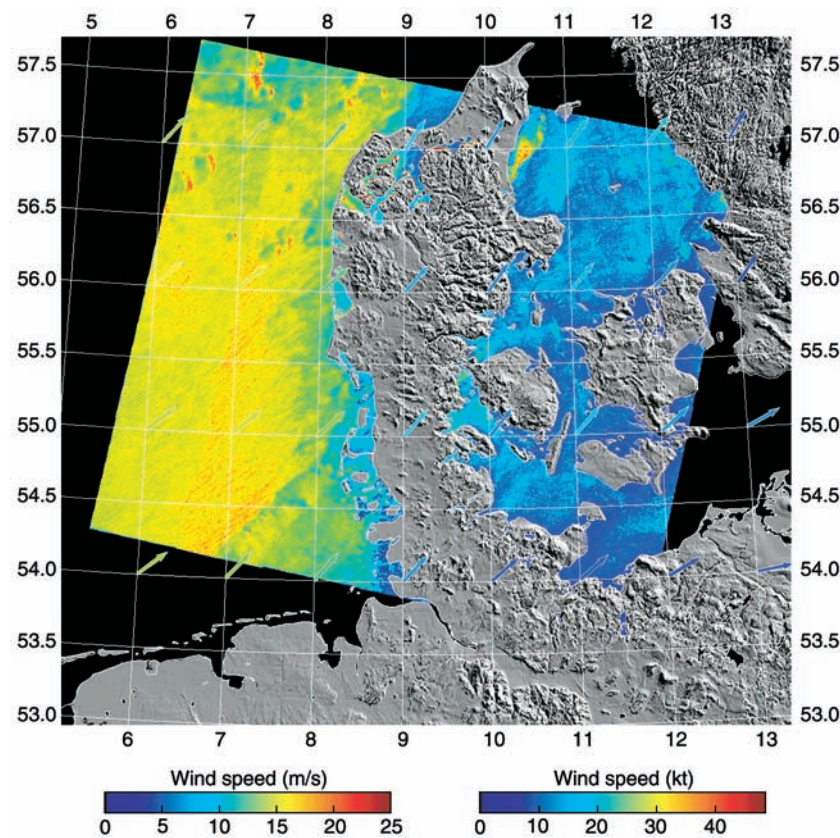


Figure 7. Wind speed image derived from an ENVISAT ASAR scene acquired in wide-swath mode over Denmark on 6 October 2004.

planned near existing farms to allow shared grid connections and reduced construction costs. At Horns Rev in southwest Denmark, for example, 80 wind turbines are currently operating and a new array of turbines, Horns Rev II, will be constructed in the near future. It is crucial that shadowing effects from one wind farm to the other are avoided by placing turbine arrays sufficiently far apart. The question, however, is: What distance is sufficient?

The mean wind speed decreases as energy is taken out of the flow by wind turbines. From modeling and *in situ* measurements near smaller wind farms, we know that a significant reduction is found between the first and second turbine in a row aligned with the wind vector.³² Additional turbines only cause a minor decrease in the mean wind speed. For large arrays of turbines, flow patterns are more complex because interaction occurs in two dimensions.

The region downstream of a wind farm is generally characterized by reduced wind speed and increased turbulence and is often called the “wind wake.” The extent and magnitude of wind wakes depend on the ambient wind speed, atmospheric stability, and the spacing of the turbines. Preliminary wake models suggest that downstream of an offshore wind farm, wind speed recovers to within 2% of the ambient wind speed over a distance of 5–14 km.³³

To measure changes in velocity as the wind passes through a large offshore wind farm, spatial information on wind speed is also needed. Provided that the accuracy of SAR wind fields is sufficient, we can derive such information from satellite SAR images.

The existing wind farm at Horns Rev appears on the NRCS SAR image obtained by the ERS-2 satellite in March 2003, as shown in Fig. 8. Single wind turbines, with a total height of 110 m, rotor diameter of 80 m, and spacing of 560 m, are distinguished in the image because of their very high radar cross section compared to the sea surface. The scene was obtained on a calm day and, as is evident from the figure, sea surface scattering is almost absent near the wind farm. Bright features in other parts of the sea, and near the shoreline in particular, are not associated with the wind. They may result from surfactants in the water or from variations in sea surface temperature. The atmospheric boundary layer is almost certainly stable near the wind farm whereas bright regions may indicate unstable atmospheric

conditions associated with higher ocean surface roughness.

The extraction of mean wind speeds near and within a wind farm from satellite SAR is done as follows. Spatial averages of wind speed are calculated within boxes lined up parallel with the wind vector. The box outline is superimposed on a grayscale wind map as shown in Fig. 9. One transect of boxes coincides in space with the wind farm at Horns Rev, whereas the other transect is shifted 8 km to the southwest where no influence of wind turbines is expected. In boxes that include wind turbines, mean winds are calculated after removing high scattering (noise) from the wind turbines. Practically, a mask is applied that eliminates pixels within a 100-m radius of each individual turbine.

In Fig. 10, we plot mean winds as a function of distance from upwind of the wind farm, through the wind farm, to downwind of the wind farm. Also plotted are mean winds obtained in the parallel, nonobstructed transect. A mean wind speed of 7.0 m/s is found just upstream of the wind farm; this is considered the free-stream velocity. At 2.5 km downstream of the last turbine, wind speed has decreased to 6.1 m/s. From this point, the wind speed gradually increases with distance until a velocity near the free-stream velocity is found approximately 7 km downstream of the last turbine. The nonobstructed transect 8 km farther to the

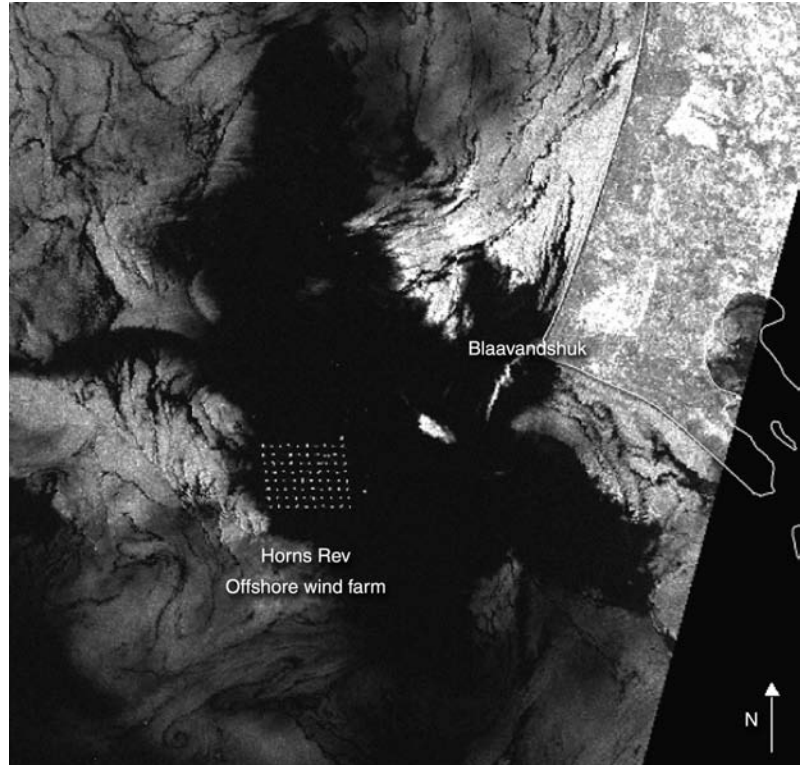


Figure 8. Subsection (50 × 50 km) of an ERS-2 SAR NRCS image acquired over Horns Rev in southwest Denmark on 16 March 2003. Conditions are calm and wind turbines are easily distinguished from the sea surface.

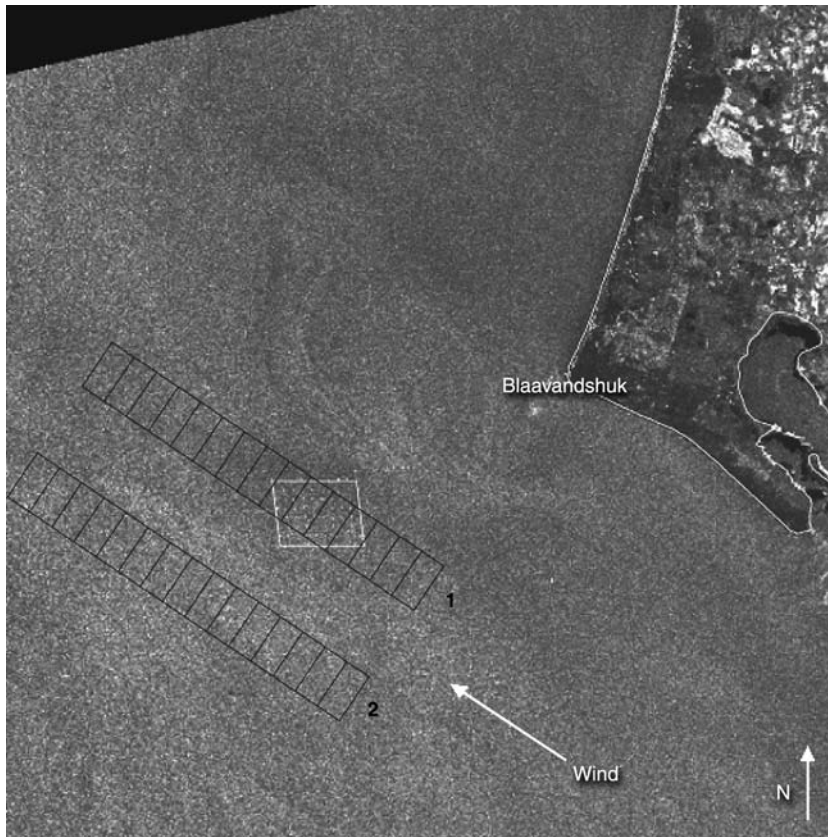


Figure 9. Subsection (50 × 50 km) of a wind speed map derived from the ERS-2 SAR imager acquired over Horns Rev on 1 March 2003. Transects are parallel to the wind vector (black boxes), and the wind farm location is indicated (white box).

southwest shows only moderate fluctuations of mean wind speed with distance. The wind speed is generally a little higher in this transect, possibly because of the longer fetch (i.e., a longer distance to shore) or random variations of the wind.

The wind speed reduction of approximately 1 m/s found downstream of the wind farm at Horns Rev is

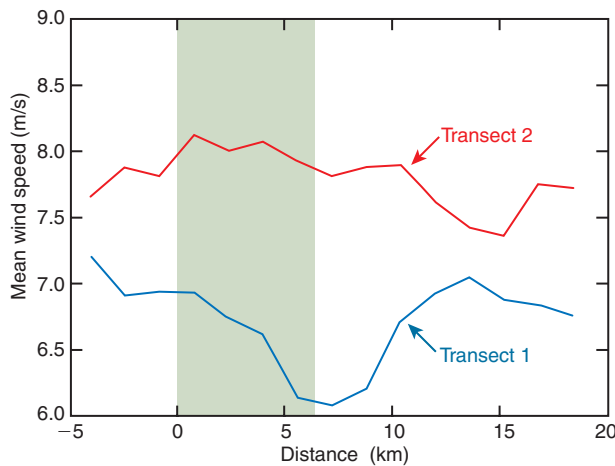


Figure 10. Mean wind speed calculated for the two transects of boxes shown in Fig. 9.

smaller than the accuracy of wind retrievals from SAR (about 1.8 m/s). However, the mean wind calculated within boxes results from 300 to 500 samples per box, which reduces uncertainty significantly. We can therefore assume that variations found are attributable to actual variations in the wind field rather than image noise. The downstream distance over which wind wakes are detected is 7 km from the last turbine. This is within the interval predicted by wake models. The results obtained are promising in terms of identifying wind wakes from SAR-derived wind speed maps. As more SAR images containing wind turbine arrays become available, it will be possible to characterize wake behavior under various wind conditions and assist wake modelers in predicting the effect of large offshore wind farms on the local wind climate.³⁴

CONCLUSION AND FUTURE PROSPECTS

In this article, we have briefly described the basic principles that allow remote measurements of the near-surface wind field over the ocean surface. In particular, we have shown how the high-resolution imaging capability of SAR scatterometry can provide a powerful complement to more conventional wind retrieval techniques. Two specific practical examples where the high-resolution capability of SAR is important have been discussed in detail. The first example presents preliminary findings from an ongoing research project sponsored by NSF to investigate barrier jets and gap flows in the Gulf of Alaska. We have shown how the high-resolution SAR wind maps collected in conjunction with this project can be extremely valuable, not only for characterizing these phenomena but also for validating mesoscale meteorological models that are difficult to check by any other means. Our second example illustrates a practical use of SAR wind mapping concerning the design and deployment of wind farms in shallow-water coastal regions for the production of electrical energy. In this example, we show how SAR wind maps can help to characterize the wind field near the turbines in the farm, particularly the downstream wake. Such characterization is important for determining turbine spacing in an individual wind farm as well as the optimal separation between two different farms.

The use of high-resolution SAR wind mapping is just beginning to be recognized. A major objective of this article is to illustrate its capability through examples from both research and application. Although much work remains to be done in the validation and refinement of SAR wind mapping techniques, the potential payoff is well worth continued effort.

ACKNOWLEDGMENTS: This study was supported and monitored by the NOAA Office of Research and Applications under contract number N00024-03-D-6606 and the Office of Naval Research National Ocean Partnership Program under contract number 661525. The views, opinions, and findings contained in this article are those of the authors and should not be construed as an official NOAA, Navy, or U.S. government position, policy, or decision.

REFERENCES

- ¹Beckmann, P., and Spizzichino, A., *The Scattering of Electromagnetic Waves from Rough Surfaces*, Macmillan, New York (1963).
- ²Ulaby, F. T., Moore, R. K., and Fung, A. K., *Microwave Remote Sensing: Active and Passive—Volume II: Radar Remote Sensing and Surface Scattering and Emission Theory*, Addison-Wesley Publishing Company, (1982).
- ³Voronovich, A. G., *Wave Scattering from Rough Surfaces*, 2nd Ed., Springer-Verlag, Heidelberg, Germany (1994).
- ⁴Fung, A. K., *Microwave Scattering and Emission Models and Their Applications*, Artech House, Norwood, MA (1994).
- ⁵Elfouhaily, T. M., Thompson, D. R., Freund, D. E., Vandemark, D., and Chapron, B., "A New Bistatic Model for Electromagnetic Scattering from Perfectly Conducting Random Surfaces: Numerical Evaluation and Comparison with SPM," *Waves Random Media* **11**, 33–43 (2001).
- ⁶Elfouhaily, T. M., Guignard, S., and Thompson, D. R., "A Practical Second-Order Electromagnetic Model in the Quasi-Specular Regime Based on the Curvature of a 'Good-Conducting' Scattering Surface," *Waves Random Media* **13**, L1–L6 (2003).
- ⁷Stoffelen, A. C. M., and Anderson, D. L. T., "ERS-1 Scatterometer Data Characteristics and Validation of the Transfer Function: CMOD4," *J. Geophys. Res.* **102**, 5767–5780 (1997).
- ⁸Spencer, W. M., Wu, C., and Long, D. G., "Improved Resolution Backscatter Measurements with the Seawinds Pencil-Beam Scatterometer," *IEEE Trans. Geosci. Remote Sens.* **38**, 89–104 (2000).
- ⁹Raney, R. K., Luscombe, A. P., Langham, E. J., and Ahmed, S., "RADARSAT," in *Proc. IEEE* **79**(6), 839–849 (Jun 1991).
- ¹⁰Brown, R. A., "Longitudinal Instabilities and Secondary Flows in the Planetary Boundary Layer: A Review," *Rev. Geophys.* **18**, 683–697 (1980).
- ¹¹Gerling, T. W., "Structure of the Surface Wind Field from the Seasat SAR," *J. Geophys. Res.* **91**(C2), 2308–2320 (1986).
- ¹²Horstmann, J., Kock, W., Lehner, S., and Tonboe, R., "Wind Retrieval over the Ocean Using Synthetic Aperture Radar with C-Band HH Polarization," *IEEE Trans. Geosci. Remote Sens.* **38**(5), 2122–2131 (2000).
- ¹³Wackerman, C. C., Rufenach, R., Johannessen, J., and Davison, K., "Wind Vector Retrieval Using ERS-1 Synthetic Aperture Radar Imagery," *IEEE Trans. Geosci. Remote Sens.* **34**, 1343–1352 (1996).
- ¹⁴Monaldo, F. M., Thompson, D. R., Beal, R. C., Pichel, W. G., and Clemente-Colón, P., "Comparison of SAR-derived Wind Speed with Model Predictions and Buoy Comparisons," *IEEE Trans. Geosci. Remote Sens.* **39**(12), 2587–2600 (Dec 2001).
- ¹⁵Monaldo, F. M., Thompson, D. R., Pichel, G., and Clemente-Colón, P., "A Systematic Comparison of QuikSCAT and SAR Ocean Surface Wind Speeds," *IEEE Trans. Geosci. Remote Sens.* **42**(2), 283–291 (Feb 2004).
- ¹⁶Overland, J. E., and Bond, N., "The Influence of Coastal Orography: The Yakutat Storm," *Monthly Wea. Rev.* **121**, 1388–1397 (1993).
- ¹⁷Pichel, W. G., and Clemente-Colón, P., "NOAA CoastWatch SAR Applications and Demonstration," *Johns Hopkins APL Tech. Dig.* **21**(1), 49–57 (Jan 2000).
- ¹⁸Loescher, K. A., Young, G. S., Colle, B. A., and Winstead, N. S., "Climatology of Barrier Jets Along the Alaskan Coast, Part I: Spatial and Temporal Distributions," *Monthly Wea. Rev.* (in press, 2005).
- ¹⁹Parish, T. R., "Barrier Winds Along the Sierra-Nevada Mountains," *J. Appl. Meteorol.* **21**, 925–930 (1982).
- ²⁰Chen, W. D., and Smith, R. B., "Blocking and Deflection of Airflow by the Alps," *Monthly Wea. Rev.* **133**, 2578–2597 (1987).
- ²¹Bell, G. D., and Bosart, L. F., "Appalachian Cold Air Damming," *Monthly Wea. Rev.* **116**, 137–161 (1988).
- ²²Doyle, J. D., "The Influence of Mesoscale Orography on a Coastal Jet and Rainband," *Monthly Wea. Rev.* **121**, 1493–1513 (1997).
- ²³Yu, C.-K., and Smull, B. F., "Airborne Observations of a Landfalling Cold Front Upstream of Steep Coastal Orography," *Monthly Wea. Rev.* **128**, 674–692 (2000).
- ²⁴Mass, C. F., and Ferber, G. K., "Surface Pressure Perturbations Produced by an Isolated Mesoscale and Topographic Barrier, Part I: General Characteristics and Dynamics," *Monthly Wea. Rev.* **118**, 2579–2596 (1990).
- ²⁵Neiman, P. J., Persson, P. O. G., Ralph, F. M., Jorgensen, D. P., White, A. B., and Kingsmill, D. E., "Modification of Fronts and Precipitation by Coastal Blocking During an Intense Landfalling Winter Storm in Southern California: Observations During CALJET," *Monthly Wea. Rev.* **132**, 242–273 (2004).
- ²⁶Colle, B. A., Loescher, K. A., Young, G. S., and Winstead, N. S., "Climatology of Barrier Jets Along the Alaskan Coast, Part II: Large-Scale and Sounding Composites," *Monthly Wea. Rev.* (in press, 2005).
- ²⁷Troen, I., and Petersen, E. L., *European Wind Atlas*, Risø National Laboratory, Roskilde, Denmark (1989).
- ²⁸Hasager, C. B., Barthelmie, R. J., Christiansen, N. B., Nielsen, M., and Pryor, S. C., "Quantifying Offshore Wind Resources from Satellite Wind Maps: Study Area the North Sea," in *Proc. 2004 European Wind Energy Conf. and Exhibition*, London, pp. 29–33 (Nov 2004).
- ²⁹Nielsen, M., Astrup, P., Hasager, C. B., Barthelmie, R. J., and Pryor, S. C., *Satellite Information for Wind Energy Applications*, Tech. Rep. Risø-R-1479(EN), Risø National Laboratory, Roskilde, Denmark (2004).
- ³⁰Barthelmie, R. J., and Pryor, S. C., "Can Satellite Sampling of Offshore Wind Speeds Realistically Represent Wind Speed Distributions?" *J. Appl. Meteorol.* **42**(1), 83–94 (2003).
- ³¹Hasager, C. B., Dellwik, E., Nielsen, M., and Furevik, B. R., "Validation of ERS-2 SAR Offshore Wind-speed Maps in the North Sea," *Int. J. Remote Sens.* **25**, 3817–3841 (2004).
- ³²Crespo, A., Hernandez, J., and Frandsen, S., "Survey of Modelling Methods for Wind Turbine Wakes and Wind Farms," *Wind Energ.* **2**, 1–24 (1999).
- ³³Barthelmie, R. J., and Pryor, S. C., "Challenges in Predicting Power Output from Offshore Wind Farms," *J. Energy Engineer.* (2005).
- ³⁴Christiansen, M. B., and Hasager, C. B., "Wake Effects of Large Offshore Wind Farms Identified from Satellite SAR," *Remote Sens. Environ.* **98**, 251–268 (2005).

THE AUTHORS

Frank M. Monaldo is the Program Manager for a NOAA effort to port APL-developed software, which converts spaceborne synthetic radar imagery into subkilometer resolution maps of the marine wind field, for use at the Center for Southeastern Tropical Advanced Remote Sensing of the University of Miami. This work provides an opportunity to validate such wind fields in hurricane-prone regions. Mr. Monaldo serves as Acting Supervisor of the Space Department's Ocean Remote Sensing Group. He received both his B.A. and M.S. degrees in physics from the Catholic University of America. In 1980, he was a visiting scientist at the Max Planck Institute for Meteorology in Hamburg, Germany. **Donald R. Thompson** received a Ph.D. degree in theoretical physics from the University of Minnesota, Minneapolis, in 1968. Dr. Thompson spent the early years of his career studying problems in few-body nuclear reactions and stellar nucleosynthesis at the California Institute of Technology, the University of Minnesota, and the Universität Tübingen in Germany. He has been at APL since 1980, focusing on problems involving electromagnetic scattering theory, ocean surface wave physics, and air-sea interactions. **Nathaniel S. Winstead** is a member of the Senior Professional Staff in APL's Ocean Remote Sensing Group. Dr.



Frank M. Monaldo



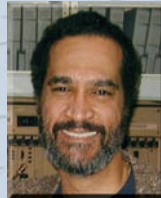
Donald R. Thompson



Nathaniel S. Winstead



William G. Pichel



Pablo Clemente-Colón



Merete B. Christiansen

Winstead's primary research focus is the study of mesoscale meteorology using SAR. He is currently the Principal Investigator on an NSF-sponsored project to study barrier jets and other mesoscale coastal flows in the Gulf of Alaska using SAR. **William G. Pichel** is a physical scientist in the Office of Research and Applications within the National Environmental Satellite, Data, and Information Service (NESDIS) of NOAA. As Chair of the Sea Surface Roughness Science Team, he leads the development and demonstration of coastal and open-ocean SAR products within NESDIS. **Pablo Clemente-Colón** serves as Chief Scientist of the U.S. National Ice Center and leads the center's Polar Science Team. Dr. Clemente-Colón also serves as an oceanographer with the NESDIS Office of Research and Applications, where he has provided remote sensing expertise in areas of satellite oceanography that include sea ice, sea surface roughness, sea surface temperature, ocean color, ocean winds, remote sensing fisheries, upper ocean dynamics, marine boundary layer processes, and multisensor data fusion. **Merete B. Christiansen** (M.Sc.) is a Ph.D. student in the Wind Energy Department at Risø National Laboratory, Denmark, where she works on the application of radar remote sensing to wind energy development. She collaborated with the Ocean Remote Sensing Group during her visit as a guest scientist at APL in 2004–2005. For further information, contact Frank Monaldo at frank.monaldo@jhuapl.edu.